Next Materials 9 (2025) 101175

Contents lists available at ScienceDirect

Next Materials

journal homepage: www.sciencedirect.com/journal/next-materials

Research article

Strain engineering in molybditene: A theoretical insight into the 2D phase of α-MoO_3

José A.S. Laranjeira [a], Fredy M. Gonzalo [a], Victor J.R. Rivera [a], Luis A. Cabral [b], Pablo A. Denis [c], Julio R. Sambrano [a,*]

[a] Modeling and Molecular Simulation Group, São Paulo State University, School of Sciences, Bauru, SP, Brazil
[b] Department of Physics and Meteorology, São Paulo State University, School of Sciences, Bauru, SP, Brazil
[c] Computational Nanotechnology, DETEMA, Facultad de Quimica, UDELAR, Montevideo 1157, 11800, Uruguay

ARTICLE INFO

Keywords:
Two-dimensional
2D
MoO_3
Few-layered
DFT
Molybditene

ABSTRACT

This first-principles study explores the structural, thermal, mechanical, electronic, optical, and vibrational properties of molybditene, the 2D phase of α-MoO_3 with $P2_1/m$ symmetry. The structure is stable at near room temperature and meets the Born–Huang mechanical criteria. Molybditene shows anisotropic mechanical properties, with Young's modulus between 84.33 and 138.48 N/m, and Poisson's ratio from 0.14 to 0.23. It has an indirect band gap with a valence band maximum at the S point and a conduction band minimum at Γ, varying from 1.75 eV (PBE) to 2.95 eV (HSE06). Light polarized along x shows visible range absorption and a peak around 3.50 eV, while y-polarized light is mainly active in the ultraviolet. Strain engineering shows a significant band gap change under the y-strain, from 1.10 to 2.30 eV, while the gap remains stable under the x-strain. Infrared and Raman spectra identify key vibrational modes at 713.06 cm^{-1} and 708.39 cm^{-1} , respectively. Notably, the strain also induces substantial changes in the optical response, including enhanced anisotropy and redshifts in the absorption edge, further expanding the potential of molybditene for applications in flexible electronics, strain-tunable sensors, and polarization-sensitive optoelectronic devices.

1. Introduction

Molybdenum trioxide (MoO_3) is a transition metal oxide that has attracted significant attention due to its chemical stability, low toxicity, abundance, and multifunctional properties[1–3]. It is widely explored in applications such as catalysis [4,5], gas sensing [6–8], electrochromic devices [9,10], and energy storage systems [11,12]. MoO_3 exists in several polymorphic forms, including the orthorhombic (α-MoO_3), monoclinic (β-MoO_3), and hexagonal (h-MoO_3) phases [13]. Among these, α-MoO_3 is the most thermodynamically stable at room temperature and is the most extensively studied [14]. The β and h phases are metastable and typically transform into the α-phase upon heating or prolonged storage.

α-MoO_3 features a layered structure composed of distorted [MoO_6] octahedra, which contributes to its high anisotropy and enables interlayer diffusion of ions or molecules [3]. As an n-type semiconductor, MoO_3 exhibits a wide band gap and a layered crystal structure that facilitates intercalation and ion transport, making it advantageous for various technological applications [15,16]. To tailor the structural, optical, and mechanical properties of MoO_3, various synthesis methods have been developed, including sol–gel processing [17–19], hydrothermal synthesis [20–22], microwave-assisted synthesis [23–25], solvothermal methods [26], and sonochemical approaches [27,28].

In this framework, several methods have been established for synthesizing few-layered MoO_3, such as mechanical exfoliation [29], pulsed laser deposition [30], thermal evaporation [31], sputtering [32], spray pyrolysis [33], chemical vapor deposition [34], hydrothermal synthesis [35] and electrodeposition [36]. Among these, liquid-phase exfoliation has emerged as a widely used approach for obtaining single- and few-layered structures, typically involving solvent-assisted grinding followed by sonication, either in pure solvents [37–42] or in aqueous solutions containing surfactants.

Liu et al. [43] described an efficient method for exfoliating 2D MoO_3 nanosheets through a combination of grinding and sonication. They identified a 50:50 ethanol-water mixture as the most suitable solvent system, despite each solvent being less effective on its own. The

* Corresponding author.
E-mail address: jr.sambrano@unesp.br (J.R. Sambrano).

https://doi.org/10.1016/j.nxmate.2025.101175
Received 4 June 2025; Received in revised form 20 August 2025; Accepted 3 September 2025
Available online 9 September 2025

produced 2D MoO_3 nanosheets notably improve sensor performance by providing greater sensitivity and quicker response and recovery times, due to their expanded surface area and numerous active sites.

Jeon and colleagues [44] synthesized 2D MoO_3 nanosheets by intercalating and exfoliating MoS_2, followed by oxidation with nitric acid. These nanosheets retain the 2D shape of MoS_2, with a thickness of about 70 % thinner than 9 nm, allowing for better ion diffusion than bulk MoO_3. In electrochromic devices, they provide superior optical contrast and faster switching, approaching the performance of advanced WO_3 nanostructures, thus demonstrating great potential for electrochromic applications.

Employing first-principles density functional theory (DFT) simulations, Liu and coworkers [45] predicted the high-performance hydrogen gas sensing of 2D MoO_3 doped with Pt or Rh. Upon exposure to oxygen in the air, the band gap of Pt- and Rh-doped MoO_3 decreases significantly by 0.62 eV and 0.51 eV. The sensor exhibits substantial charge variations—1.487 e for oxygen adsorption and 0.394 e for hydrogen adsorption—indicating high sensitivity and a low detection limit.

DFT calculations and deformation potential theory were utilized to demonstrate that few-layer MoO_3 exhibits exceptionally high acoustic-phonon-limited carrier mobility exceeding 3000 $cm^2\ V^{-1}\ s^{-1}$ [46]. Moreover, a pronounced in-plane transport anisotropy is observed, with mobility ratios between crystallographic directions reaching 20–30. This anisotropy arises from the strong directional dependence of both the elastic modulus and the deformation potential, which are closely linked to the valence charge density distribution and the states near the band edges.

Tong et al. [47] employed first-principles calculations and the Boltzmann transport equation to investigate the phonon-limited thermal conductivity of MoO_3. Remarkably, they predicted an ultralow room-temperature in-plane thermal conductivity of 1.57 W/mK and 1.26 W/mK along the two principal crystallographic directions—values significantly lower than those of most known 2D materials. This behavior is attributed to soft flexural and acoustic phonon modes coupled through the finite thickness, as well as to pronounced anharmonic lattice interactions that enable strong three- and four-phonon scattering. These findings position MoO_3 as a promising material for thermoelectric applications.

The present work presents a characterization of the 2D phase of molybdenum trioxide, which we will refer to as molybditene, through first-principles DFT calculations. The study includes an examination of the electronic structure via band structure analysis and density of states. Additionally, mechanical and optical properties will be investigated, along with an evaluation of the effects of uniaxial strain on the structural and electronic features of molybditene.

2. Computational Setup

In this study, all computational analyses were executed using the Vienna ab initio simulation package (VASP) [48]. The generalized gradient approximation (GGA), based on the Perdew, Burke, and Ernzerhof (PBE) functional [49,50], was employed to calculate the exchange-correlation energies, while the projector augmented wave (PAW) method [50] accounted for interactions between core and valence electrons. Electronic states were described using plane waves, and the plane wave cutoff energy was chosen at 520 eV. To avoid interlayer interactions, a 15 Å vacuum layer was added along the c-axis. For the Brillouin zone, structural optimization (partial density of states) was performed on a 5 × 5 × 1 (18 ×18 x 1) Gamma-centered **k**-point grid. Structural optimizations were carried out using the conjugate-gradient algorithm until the convergence criteria were satisfied, which involved energy deviations for atomic positions and lattice parameters being below 10^{-5} eV, and Hellmann–Feynman forces per atom not exceeding 0.015 eV/Å. To comprehensively evaluate the thermodynamic stability of molybditene, ab initio molecular dynamics (AIMD) simulations were performed [51,52]. To a more accurate description of the electronic band gap, the HSE06 functional [53] was utilized. For this functional, the structure was optimized employing a coarser 3 × 3 × 1 k-point mesh. Subsequently, a denser mesh of 9 × 9 × 1 mesh was considered for band structure calculations.

Vibrational analysis at the Γ point was carried out via numerical second derivatives of the total energies estimated with the coupled perturbed HF/Kohn–Sham algorithm [54] implemented in CRYSTAL17 software [55]. The structural parameters, including average bond lengths (l_{av}), distortion index (D), polyhedral volume (V), and effective coordination number (ECoN), were collected using the VESTA software [56].

The elastic constants (C_{ij}) were determined by taking the second derivative of the energy (E) with respect to the strain components (ϵ_i and ϵ_j), as described by the following equation:

$$C_{ij} = \partial^2 E / \partial\epsilon_i \partial\epsilon_j \tag{1}$$

The orientation-dependent behavior of Young's modulus (Y), shear modulus (G), and Poisson's ratio (ν) was obtained through the following expressions [57]

$$1/E(\theta) = S_{11}c^4 + S_{22}s^4 + 2S_{16}c^3s + 2S_{26}cs^3 + (S_{66} + 2S_{12})c^2s^2 \tag{2}$$

$$\nu(\theta)/E(\theta) = (S_{66} - S_{11} - S_{22})c^2s^2 - S_{12}\left(c^4 + s^4\right) + (S_{26} - S_{16})(cs^3 - c^3s) \tag{3}$$

$$1/4G(\theta) = (S_{11} + S_{22} - 2S_{12})c^2s^2 + S_{66}(c^2 - s^2)^2 \Big/ 4 - (S_{16} - S_{26})(c^3s - cs^3) \tag{4}$$

where $s = \sin\theta$, $c = \cos\theta$, and $\theta \in [0,\ 2\pi]$ is the angle with respect to the $+x$ axis. $S_{ij} = C_{ij}^{-1}$ are the elastic compliance constants.

To quantify the mechanical anisotropy, we evaluated the angular dependence of the in-plane Young's modulus (Y), shear modulus (G), and Poisson's ratio (ν), the degree of anisotropy was quantified by the ratio (η_P)

$$\eta_P = \frac{P_{\max}}{P_{\min}} \tag{5}$$

where P denotes Y, G or ν. This dimensionless ratio provides a straightforward metric to assess the directional variation of each property and the extent of anisotropy in the 2D material.

The energetic stability of the molybditene was evaluated by computing its cohesive energy (E_{coh}), which is defined by:

$$E_{coh} = \left(E_{\text{Molybditene}} - \sum_i n_i E_i\right) \Big/ \sum_i n_i, \tag{6}$$

where $E_{\text{Molybditene}}$ is the total energy of the molybditene structure, E_i is the energy of an isolated atom i (Mo and O), and n_i is the number of i atoms in the sheet.

The optical properties were calculated within the independent particle approximation (IPA) using the LOPTICS = .TRUE. flag in the VASP code. In this approach, the imaginary part of the frequency-dependent dielectric tensor is computed from direct interband transitions, following the formalism outlined by Gajdoš et al. [58]. The summation involves transitions between occupied valence and unoccupied conduction bands at each **k**-point, requiring a sufficiently dense **k**-point mesh (18 ×18 x 1) and an increased number of empty bands (typically two to three times the number of occupied bands) to ensure convergence.

In this approach, the optical absorption coefficient α(ω) was determined from the complex dielectric function ε(ω), which describes the frequency-dependent response of the electronic system to an external electromagnetic field. The dielectric function is defined as

$$\varepsilon(\omega) = \mathrm{Re}[\varepsilon(\omega)] + i\mathrm{Im}[\varepsilon(\omega)], \tag{7}$$

where $\mathrm{Re}[\varepsilon(\omega)]$ represents the dispersive part associated with energy storage, and $Im[\varepsilon(\omega)]$ accounts for optical losses due to absorption. The absorption coefficient can then be expressed as

$$\alpha(\omega) = \sqrt{2}\left[(\mathrm{Re}[\varepsilon(\omega)])^2 + (Im[\varepsilon(\omega)])^2)^{1/2} - \mathrm{Re}[\varepsilon(\omega)]\right]^{1/2} \quad (8)$$

This formulation highlights the direct relationship between the frequency-dependent dielectric response and the absorption of electromagnetic radiation in the material, providing valuable insights into its optoelectronic performance.

3. Results and Discussion

3.1. Structure and Stability

Molybditene adopts a monoclinic structure that crystallizes in the $P2_1/m$ space group (No. 11), as illustrated in Fig. 1. The optimized lattice parameters are a = 3.95 Å and b = 3.70 Å. These values are closer to the reported by Zhang and Lai [46] for MoO_3 monolayer (a = 3.721 Å and b = 3.919 Å) at the optB88-vdW level. Its structure is composed of distorted [MoO_6] octahedra, with an average Mo–O bond length of approximately 2.00 Å and an effective coordination number (*ECoN*) of 3.42. The deviation between the ideal coordination number (6 for octahedral geometry) and the calculated ECoN indicates a significant distortion within the coordination polyhedron, reflecting the pronounced structural distortion of the [MoO_6] units. This two-dimensional phase can be derived from the exfoliation of a single layer of α-MoO_3. The computed cohesive energy (E_{coh}) is −5.60 eV/atom, confirming the energetic stability of this 2D material with respect to its isolated atomic constituents.

To evaluate the thermal stability of monolayer MoO_3 , we performed *ab initio* molecular dynamics (AIMD) simulations at 300 K using a 3 × 3 × 1 supercell over a timescale of 10 ps. The total energy profile, shown in Fig. 2a, exhibits only moderate fluctuations around a well-defined average value, with no signs of structural degradation or bond breaking throughout the simulation. This energy behavior indicates thermodynamic equilibrium and good structural resilience at room temperature.

Fig. 2b and c compare the atomic configurations before and after the simulation, respectively. The final structure maintains the overall crystallographic arrangement, confirming the structural integrity of the monolayer under thermal perturbation. However, small distortions are observed, particularly among the oxygen atoms, which exhibit slight displacements due to thermal motion. These results collectively demonstrate that monolayer MoO_3 possesses excellent thermal stability, with only minor structural distortions upon thermal excitation.

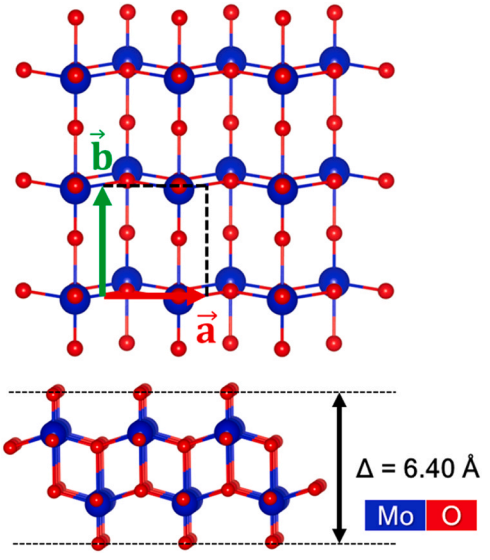

Fig. 1. Top and side views of a representative unit cell of molybditene, with the lattice vectors indicated. The structure exhibits a thickness of approximately 6.40 Å.

The phonon dispersion was calculated to analyze the dynamical stability of the novel structure, as represented in Fig. 3. One negative phonon mode with a minimum frequency of −0.27 THz (-9.00 cm^{-1}) at Γ → X direction. Such small imaginary frequencies could be an artifact of limited supercell size considered (3 ×3×1 supercell), **k**-points, or reflect the lattice instability over large wave undulations. Wang et al. [59] define −2 THz in the phonon vibration frequency as the limit for free-standing monolayers.

3.2. Mechanical Properties

The mechanical properties of molybditene were systematically investigated through first-principles calculations, and the elastic constants were obtained as C_{11} = 142.99 N/m, C_{12} = 19.81 N/m, C_{22} = 87.08 N/m, and C_{66} = 41.05 N/m. These values fulfill the Born–Huang mechanical stability criteria for two-dimensional materials with rectangular symmetry, specifically the conditions $C_{11} > 0$, $C_{66} > 0$, and $C_{11}C_{22} > C_{12}^2$, which confirms that molybditene is mechanically stable under small elastic deformations. To further analyze the anisotropic mechanical response of this monolayer, we evaluated the direction-dependent Young's modulus (*Y*), shear modulus (*G*), and Poisson's ratio (*ν*), whose polar plots are presented in Fig. 4. The calculated η_Y, η_G, and η_ν were 1.64, 1.09, and 1.64 respectively, indicating a moderate degree of mechanical anisotropy. Compared to other well-known 2D materials, monolayer MoO_3 exhibits moderate in-plane stiffness. Its maximum Young's modulus of 138.48 N/m is higher than that of MoS_2 [60] (127.7 N/m), but significantly lower than that of graphene [61] (348 N/m) and MXene $Ti_3C_2O_2$ [62], which shows values as high as 247–319 N/m depending on the surface termination. In terms of shear modulus, MoO_3 reaches a maximum value of 44.71 N/m, which is lower than those of graphene (150 N/m) and MXene $Ti_3C_2O_2$ (105–133 N/m), but still in the range of MoS_2 (52 N/m). The Poisson's ratio of MoO_3, ranging from 0.14 to 0.23, aligns with values reported for graphene (0.17) and MoS_2 (0.22). These results position MoO_3 as mechanically competitive, particularly when compared to MoS_2, while offering anisotropic behavior potentially useful for strain-engineered applications.

3.3. Electronic Analysis

The electronic band structure and projected density of states (PDOS) are presented in Fig. 5 and Fig. 6, respectively. The results reveal that molybditene exhibits an indirect band gap, with the valence band maximum (VBM) located at the S point and the conduction band minimum (CBM) at the Γ point in the Brillouin zone. The band gap energy was determined to be 1.75 eV within the generalized gradient approximation (PBE functional) and increases to 2.95 eV when using the more accurate hybrid functional (HSE06), highlighting the importance of exchange-correlation treatment for predicting electronic behavior.

The valence band edge near the S point shows noticeable curvature and dispersion of approximately 1 eV, suggesting significant band delocalization. Similarly, the conduction band near the Γ point displays a nearly parabolic dispersion, characteristic of low effective masses. These features point to lightweight charge carriers at both band edges, which are highly desirable for optoelectronic applications due to enhanced carrier mobility and efficient optical absorption.

From the projected density of states (PDOS), it is possible to analyze the composition of the electronic states near the Fermi level and gain insights into the bonding nature in molybditene. The valence band is mainly composed of oxygen *p*-orbitals (O_p), with significant contributions from the p_x, p_y, and p_z orbitals at the VBM. This indicates that the

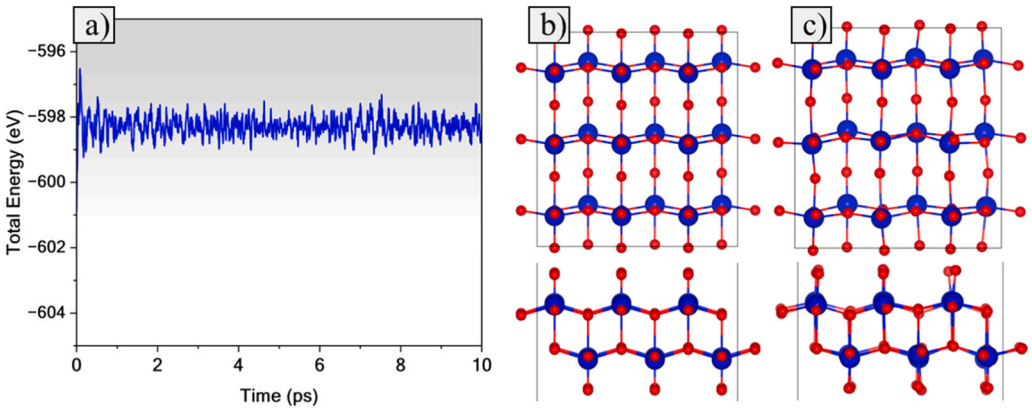

Fig. 2. Thermal stability analysis of monolayer MoO_3 via *ab initio* molecular dynamics (AIMD) at 300 K. (a) Total energy fluctuations over a 10 ps simulation using a $3 \times 3 \times 1$ supercell. (b) Top and side views of the initial atomic structure. (c) Top and side views of the final configuration after the AIMD run, revealing minor distortions and local rippling due to thermal motion.

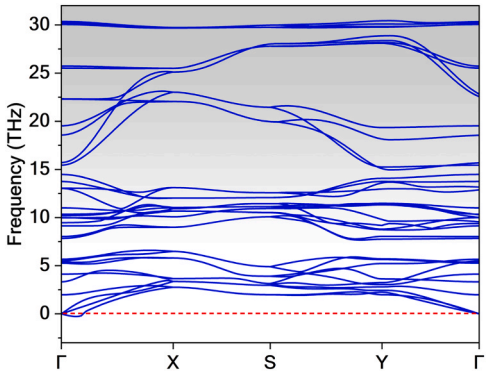

Fig. 3. Phonon dispersion along the high-symmmetry pathway in the Brillouin zone obtained for MoO_3 monolayer.

highest occupied states are mainly derived from O_p orbitals, with only minor hybridization from Mo_d orbitals. In contrast, the CBM is dominated by molybdenum *d*-orbitals, especially the d_{xy} component, with an additional notable contribution from the oxygen p_x orbital. This composition suggests that the states at the CBM arise primarily from the hybridization of Mo and O orbitals in the Mo–O bonds. Furthermore, the band structure reveals degeneracies at the VBM and CBM along certain high-symmetry directions; however, these degeneracies are lifted in other regions of the Brillouin zone. This partial symmetry breaking is attributed to distortions in the [MoO_6] octahedra, which locally perturb the crystal field and lift the degeneracy of the electronic levels.

The effective masses of electrons and holes at the CBM and VBM were calculated along the main symmetry directions of the Brillouin zone using the PBE functional. These values were obtained by fitting a second-order polynomial to the band edges, ensuring reliable results. The data are summarized in the Table 1.

As shown, the effective masses are highly anisotropic and depend strongly on the direction. Along the Γ → X direction, the electron effective mass is relatively low (0.70 m_o), indicating favorable transport for electrons, while the hole effective mass is much larger in magnitude (3.00 m_o), suggesting lower mobility for holes in this direction. Along X → S, electrons are heavier (3.37 m_o), but holes become considerably lighter (0.59 m_o). The largest electron mass appears along S → Y (10.04 m_o), which points to sluggish electronic transport in this direction, while the hole mass here is 1.71 m_o. Along Y → Γ, the electrons possess the lowest effective mass (0.66 m_o), whereas the holes exhibit the highest effective mass (5.24 m_o).

These results indicate that the material exhibits strong directional (anisotropic) transport properties. The relatively small electron effective masses along Γ → X and Y → Γ directions could be advantageous for applications that require efficient electron conduction, while the heavier masses in other directions may lead to interesting anisotropic carrier dynamics.

3.4. Optical Properties

The optical properties of molybditene were evaluated through its absorption and reflection spectrum, as illustrated in Fig. 7, revealing a pronounced anisotropic behavior characteristic of its low symmetry 2D structure. In the infrared region, the material exhibits negligible optical activity for both polarization directions, indicating transparency in this range. However, distinct differences emerge between the xx- and yy-polarized components as the photon energy increases. For the x-component, corresponding to the in-plane xx direction, the first

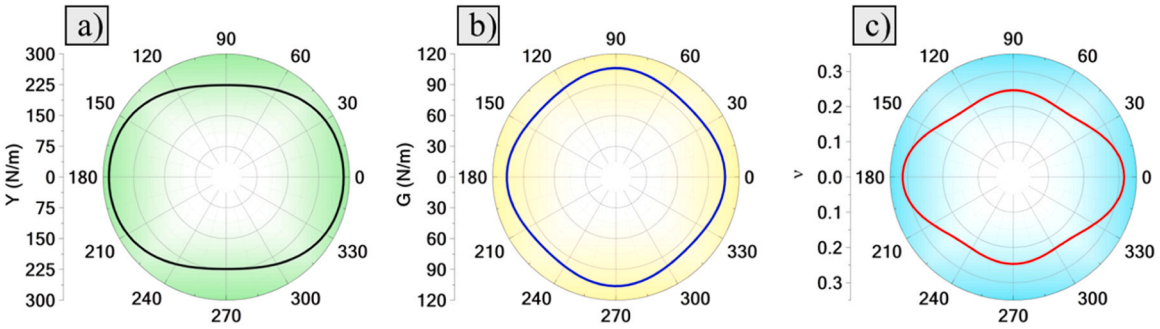

Fig. 4. Directional dependence of the mechanical properties of molybditene. Panels (a)–(c) present (a) Young's modulus (Y), (b) shear modulus (G), and (c) Poisson's ratio (ν), respectively.

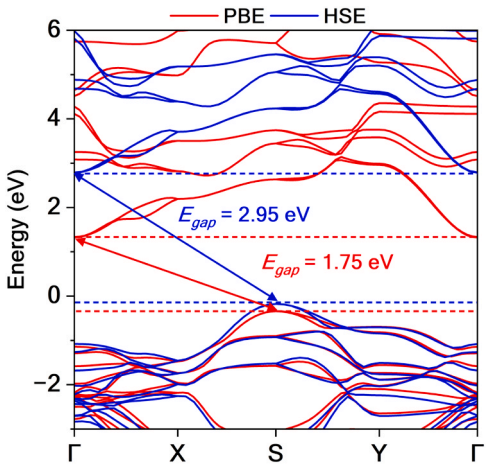

Fig. 5. Electronic band structure of molybditene calculated using the PBE (red) and HSE06 (blue) functionals. The band gap energy (E_{gap}) obtained from each method is indicated.

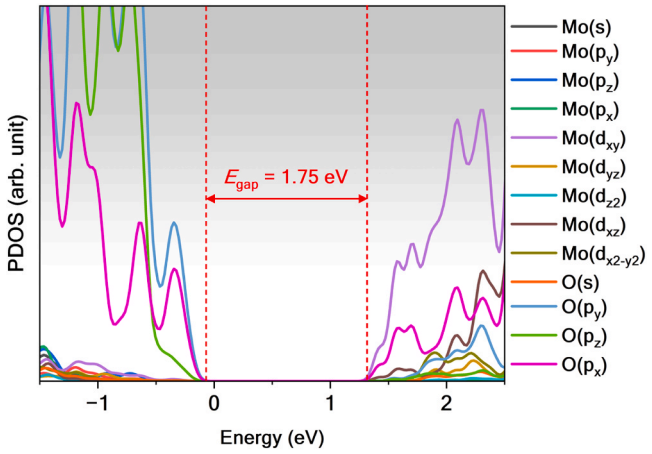

Fig. 6. Projected density of states (PDOS) of molybditene determined at PBE/GGA level. Color-coded curves distinguish the orbital contributions.

Table 1
Effective masses of electrons and holes (in units of the free electron mass, m_0) calculated along high-symmetry directions in the Brillouin zone for unstrained molybditene using the PBE functional.

Path	Electron (m^*/m_0)	Hole (m^*/m_0)
Γ → X	0.70	3.00
X → S	3.37	0.59
S → Y	10.04	1.71
Y → Γ	0.66	5.24

absorption and reflection peaks appear in the green-to-blue region of the visible spectrum (approximately 2.4–2.6 eV). The strongest absorption peak is centered around 3.5 eV.

In contrast, the y-polarized response (for yy direction) shows markedly different behavior. The first absorption peak for this component occurs in the ultraviolet region, around 3.2 eV, suggesting that molybditene presents a lower optical activity for this polarization within the visible range. The main absorption peak for the yy component appears at approximately 4.0 eV, significantly higher in energy than that of the xx component. This strong directional dependence of the optical response highlights the intrinsic optical anisotropy of molybditene, which stems from its reduced lattice symmetry and distinct electronic transitions along different crystallographic directions. Such anisotropy is closely

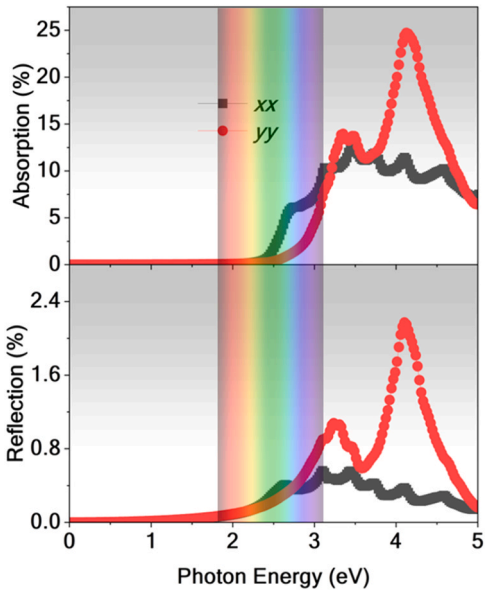

Fig. 7. Optical properties of monolayer molybdite. Panels (a) and (b) show the absorption and reflectivity spectra, respectively, for the in-plane xx (black) and yy (red) components.

related to directional variations in the optical dipole matrix elements, which govern the strength and polarization dependence of optical transitions [63].

Fig. 8 displays the real and imaginary parts of the frequency-dependent dielectric function for monolayer MoO_3, considering incident light polarized along the x (black curve) and y (red curve) crystallographic directions. The shaded region corresponds to the visible spectrum, which facilitates the interpretation of optical activity relevant to technological applications.

The real part of the dielectric function, shown in panel (a), describes the dispersive response of the material. For both polarization directions, Re[ε(ω)] increases significantly near the onset of absorption (approximately 2.2–2.5 eV), reaching prominent peaks between 2.5 and 3.2 eV. The static dielectric constant (as ω approaches zero) is moderate (closer to 4) and demonstrates optical anisotropy, with the yy component slight higher than the xx component. At higher photon energies (above 4 eV), the real part of the dielectric function becomes negative.

The imaginary part of the dielectric function, presented in panel (b), is directly associated with optical absorption due to interband electronic transitions. Im[ε(ω)] is nearly zero below the band gap for both polarization directions, confirming the absence of optical transitions in this range. The sharp absorption onset occurs around 2.4–2.6 eV, consistent with the calculated absorption, followed by prominent peaks in the visible and ultraviolet range. The most intense absorption peak for the yy polarization appears close to 4.0–4.2 eV, while for the xx direction it is lower, around 3.5 eV. These peaks are signatures of strong interband transitions and underline the highly anisotropic optical response of the material.

The differences in intensity and position of the main optical features between the xx and yy polarizations underscore the intrinsic optical anisotropy of MoO_3, which stems from its lattice structure and the directional character of the dipole-allowed electronic transitions.

3.5. Strain Response

Strain engineering was used to investigate the structural and electronic response of molybditene under mechanical deformations along the *x* and *y* directions, with uniaxial deformations ranging from –3 % to + 3 %. Key structural descriptors such as the average Mo–O bond length (l_{av}), the volume of the [MoO_6] octahedra (*V*), the distortion index (*D*),

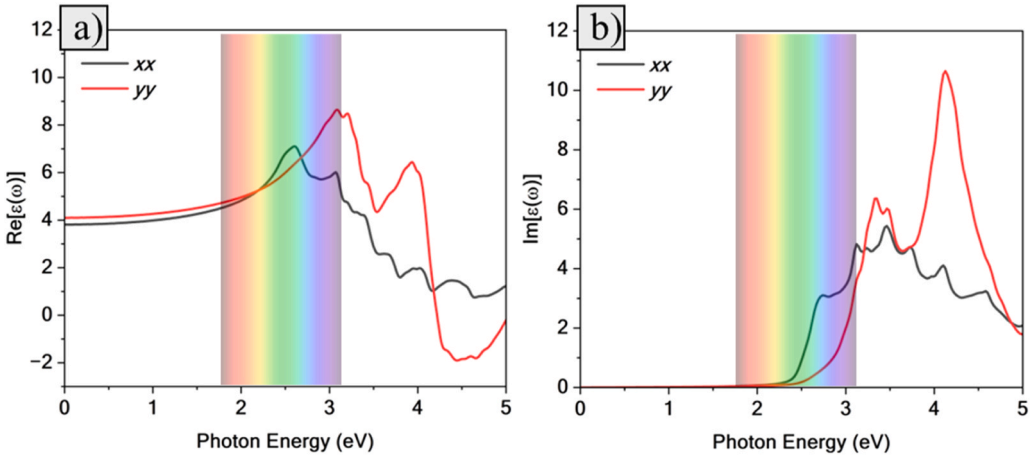

Fig. 8. Real (a) and imaginary (b) parts of the frequency-dependent dielectric function for monolayer MoO_3 under in-plane polarized light, computed using the independent particle approximation (IPA). The black and red curves represent the xx and yy polarization directions, respectively.

and the effective coordination number (*ECoN*) along with the band gap energy (E_{gap}), were evaluated under these mechanical deformations. The behavior of these parameters is summarized in Fig. 9.

Anisotropic behavior is clearly observed in the evolution of l_{av}, D, and E_{gap}. The l_{av} increases with tensile strain along the *y*-direction (ε_y). Conversely, for strain along the x-direction (ε_x), a slight reduction in l_{av} is observed, indicating a subtle bond compression. Despite these directional differences, the total variation of l_{av} remains within a narrow window (~0.015 Å). The distortion index D, which quantifies the deviation of the bond lengths on [MoO_6] octahedra from l_{av}, exhibits a similar trend. Notably, deformation along the *x*-axis leads to a decrease in D as the ε_x increases, while for the *y*-axis, notice that D increases with ε_y.

Interestingly, the E_{gap} shows a remarkable anisotropic response to strain. Along the x-direction, E_{gap} shows a moderate variation, fluctuating slightly between 1.63 and 1.83 eV. However, under y-axis strain, E_{gap} exhibits a much more significant variation, ranging from 1.10 eV to 2.30 eV approximately. This implies that uniaxial strain along the y-direction can be effectively used to tune the optical and electronic properties of molybdite, potentially enabling its use in flexible electronics, tunable optoelectronic devices, or strain sensors.

In contrast, the V and *ECoN*, which represent the spatial occupation and local bonding environment around Mo atoms, exhibit more isotropic behavior. For both ε_x and ε_y, *ECoN* decreases with increasing strain, indicating that tensile deformation leads to weaker coordination and less compact local environments. Specifically, *ECoN* ranges from 3.57 to 3.23 along the *x*-direction and from 3.72 to 3.25 along the y-direction, highlighting a progressive loss of octahedral coordination. Similarly, the volume V of the [MoO_6] units increases slightly under strain, with values varying from 10.08 $Å^3$ to 10.23 $Å^3$ (for ε_x) and from 10.06 $Å^3$ to 10.24 $Å^3$ (for ε_y).

Fig. 10 represents the band structures for molybdite under several strains at x- and y- directions. As previously discussed, deformations along the x-direction do not significantly alter the electronic structure of molybdite. The band dispersion remains nearly unchanged, and the overall topology of the valence and conduction bands is preserved, indicating a relatively rigid electronic response to strain applied in this direction. In contrast, for ε_y, a pronounced impact is noticed on the electronic band structure. With increasing tensile strain, the VBM becomes progressively flatter, especially along the S → Y path. This

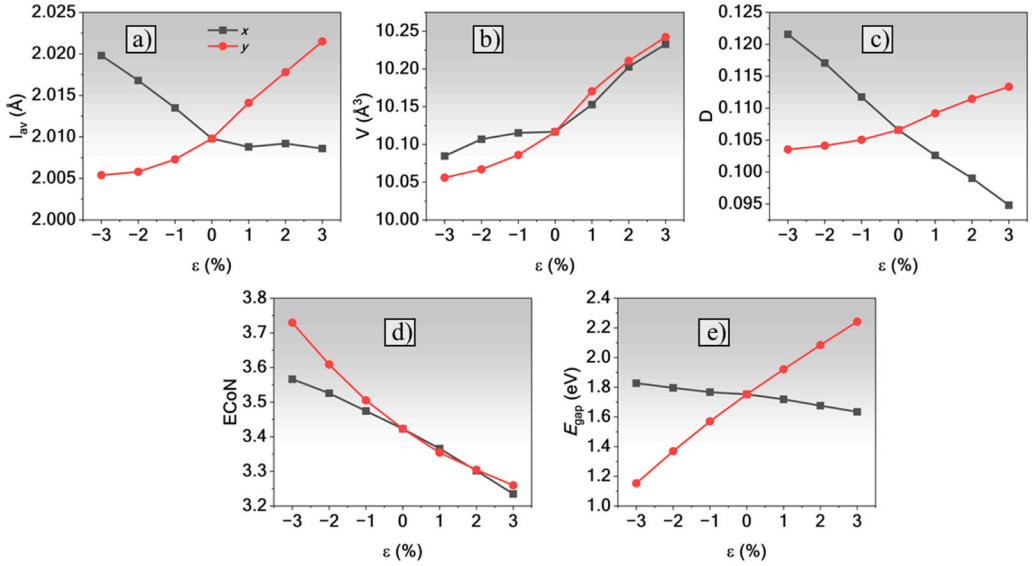

Fig. 9. Examination of structural and electronic parameters of molybdite under uniaxial strain. Panels (a)–(e) present the evolution of (a) average Mo–O bond length (l_{av}), (b) [MoO_6] octahedral volume (V), (c) distortion index (D), (d) effective coordination number (*ECoN*), and (e) band gap energy (E_{gap}) as functions of the applied strain. The results are shown for each strain condition considered along both the x- and y-directions.

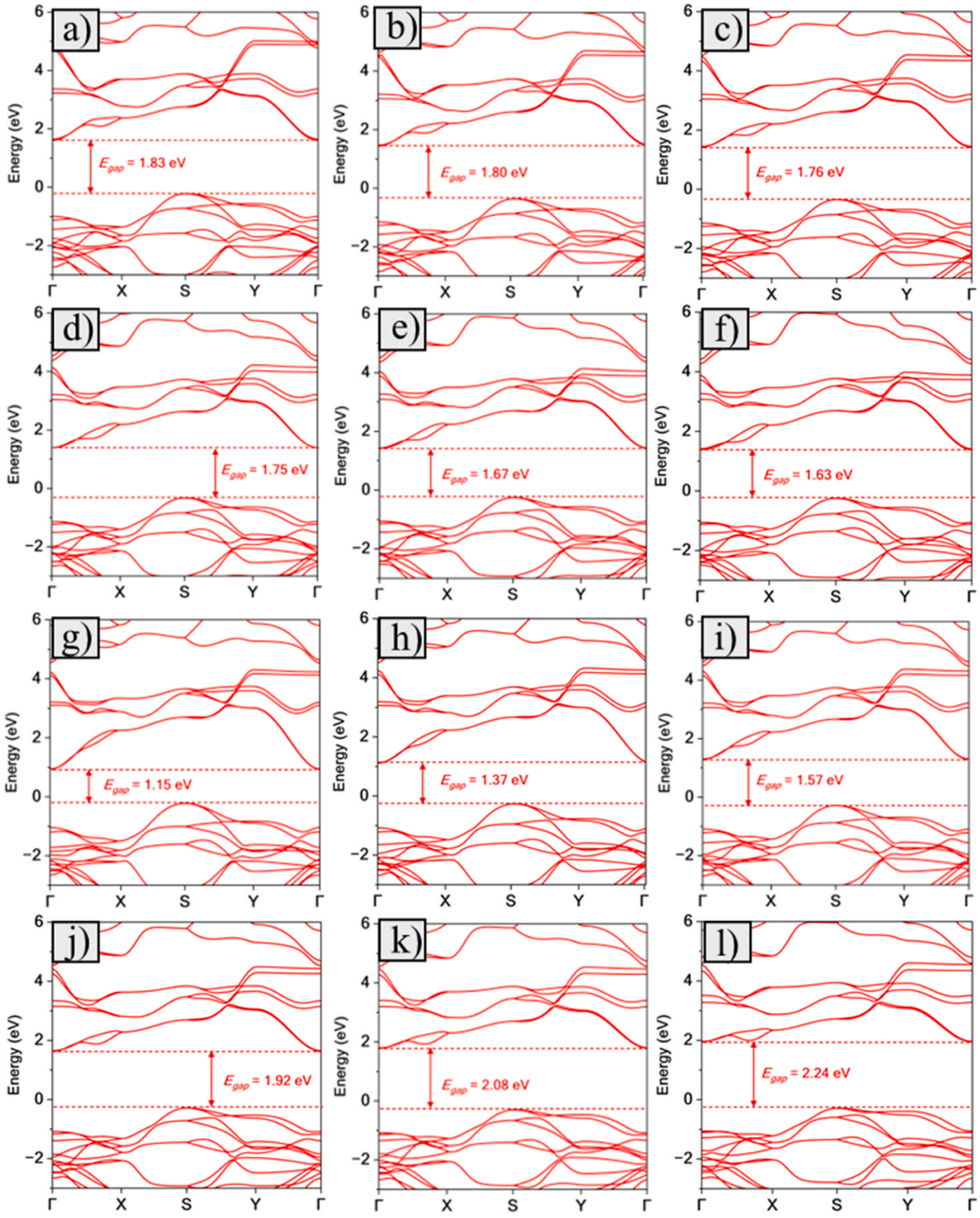

Fig. 10. Electronic band structures of molybditene under uniaxial strain. Panels (a)–(f) show the band structures for strain applied along the x-direction, with ε_x = –3 %, −2 %, –1 %, + 1 %, + 2 %, and + 3 %, respectively. Panels (g)–(l) correspond to strain along the y-direction, with ε_y = –3 %, −2 %, –1 %, + 1 %, + 2 %, and + 3 %. The band gap energy values (E_{gap}) are highlighted in each panel.

flattening is indicative of localized electronic states.

Under compressive strain along the y-axis, a different behavior is observed. The bands near the VBM and CBM become more dispersive, particularly those defining the CBM, which show a dispersion exceeding 2 eV. This suggests that compressive ε_y enhances band curvature, potentially improving electronic transport properties due to the lower effective mass of the charge carriers.

The analysis of DOS of molybditene under various uniaxial strain conditions (Fig. 11) reveals notable modifications in the electronic structure. As expected, the valence band is predominantly derived from O states, while the conduction band is mainly composed of Mo states. Under strain along the y-direction (ε_y), a clear reduction in the DOS at the CBM is observed, suggesting an increase in band dispersion and a delocalization of electronic states. This trend is consistent with previous band structure analyses, where the CBM becomes more dispersive with tensile strain along y. This mechanical perturbation introduce a short range disorder in the local environment modify the overlap between Mo_d and O_p orbitals that dominate the valence and conduction band

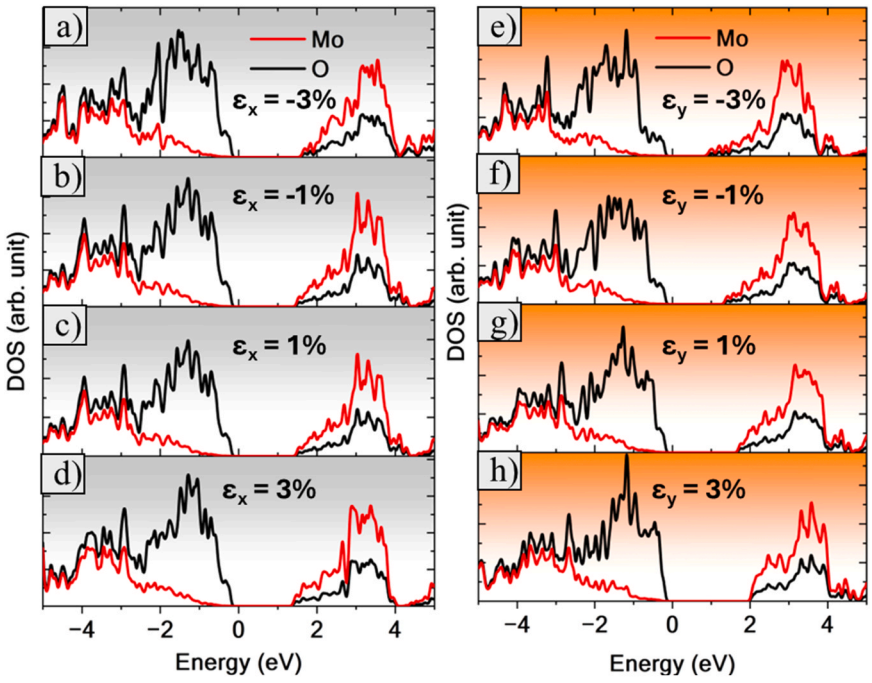

Fig. 11. Density of states (DOS) of molybditene under uniaxial strain. Panels (a)–(d) show the DOS for strain applied along the x-direction, with $\varepsilon_x = -3$ %, –1 %, + 1 %, and + 3 %, respectively. Panels (e)–(h) correspond to strain along the y-direction, with $\varepsilon_y = -3$ %, –1 %, + 1 %, and + 3 %. The Fermi level was shifted for 0 eV.

edges. As strain alters the bond angles and lengths, it tunes the degree of orbital overlap, leading to anisotropic shifts in the band gap. These changes in the electronic structure are directly correlated with the observed variations in optical absorption, as they modify the interband transition probabilities, offering a viable route for band structure engineering in optoelectronic applications.

Fig. 12 presents the optical absorption spectra of monolayer MoO_3 under uniaxial strain along the x and y directions. The intrinsic anisotropy observed in the pristine form is preserved under all strain conditions, with the absorption along the yy polarization (red curves) consistently stronger than along xx (black curves), indicating direction-dependent optical behavior.

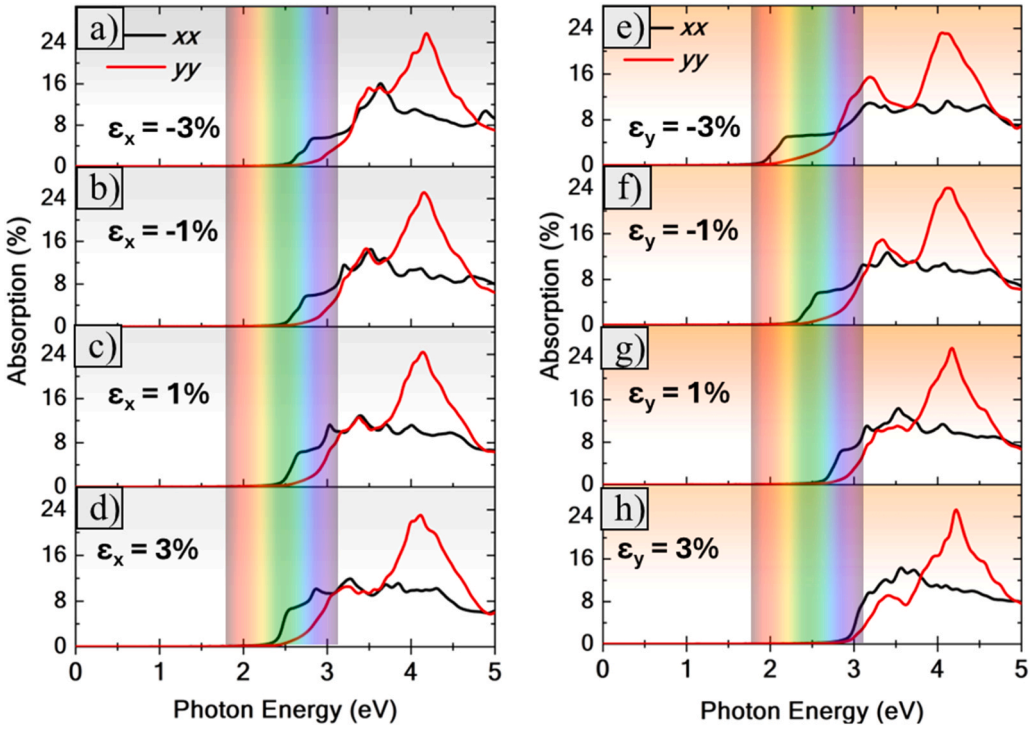

Fig. 12. Optical absorption of molybditene under uniaxial strain. Panels (a)–(d) show the DOS for strain applied along the x-direction, with $\varepsilon_x = -3$ %, –1 %, + 1 %, and + 3 %, respectively. Panels (e)–(h) correspond to strain along the y-direction, with $\varepsilon_y = -3$ %, –1 %, + 1 %, and + 3 %. The red and black line indicate the absorption for xx and yy components, respectively.

For strain applied along the x-axis (panels a–d), the absorption onset remains relatively stable, varying slightly from 2.4 to 2.5 eV as the strain increases. The position of the first absorption peak in the yy component exhibits a mild redshift, shifting from 3.4 eV at compressive strain (ε_x = –3 %) to 3.2 eV at tensile strain (ε_x = 3 %). The main absorption peak in the yy channel appears at approximately 4.1 eV and remains essentially unaffected by the applied strain. For the xx component, the most intense peak also undergoes a redshift, varying from 3.4 eV (ε_x = –3 %) to 3.2 eV (ε_x = 3 %), occurring nearly at the same energy as the first absorption peak observed in the yy component. These results shows that the mechanical perturbation along the x-direction only introduce moderate variations in the absorption spectra of molybditene.

In contrast, the application of strain along the y-axis (panels e–h) results in a marked redshift in the absorption onset for both polarization directions. Specifically, for ε_y = +3 % (panel h), the onset occurs around 3.0 eV, while for ε_y = –3 % (panel e), it drops to approximately 1.9 eV. This significant shift indicates that compressive strain along the y-direction effectively narrows the optical gap, enhancing light absorption in the lower energy region. The first absorption peak for the xx component follows this redshift trend, varying from 3.2 eV (ε_y = +3 %) to 2.2 eV (ε_y = –3 %). In contrast, for the yy component, the first absorption peak remains relatively stable, shifting only from 3.4 eV to 3.1 eV across the same strain range. A similar strain-induced modulation of the optical response has been reported for other 2D materials. For example, in BAs monolayer [64], application of tensile strain leads to a blueshift in the first optical peak and a redshift in the second peak of the imaginary part of the dielectric function (Im[ε(ω)]), with the magnitude of the shift being more pronounced for the second peak. It can be considered also the results for GeSe monolayers [65], both puckered and buckled phases. When strain is applied along the x direction, the intensity of the main absorption peak decreases and shifts toward higher energies. In the buckled structure, the first absorption peak disappears under compressive strain and moves to higher energies as tensile strain is applied. In contrast, for the puckered structure, increasing tensile strain results in a shift of the absorption edge to lower energies.

In particular, such strain-engineered control can be exploited in next-generation smart windows, strain-sensitive photodetectors [66,67], or flexible solar cells [68,69], where the optical absorption range can be dynamically adjusted in response to mechanical deformation. Moreover, the reversible and low-energy nature of the strain-induced tuning makes molybditene a suitable candidate for integration into wearable electronics and sensors that operate under variable mechanical stress conditions.

3.6. Vibrational Features

Infrared and Raman spectroscopy are powerful, complementary techniques for probing the vibrational dynamics of materials. The vibrational properties of molybditene at the Γ point were analyzed using the coupled-perturbed Hartree–Fock/Kohn–Sham (CPHF/KS) formalism, with the resulting infrared (IR) and Raman spectra presented in Fig. 13. The irreducible representation of the vibrational modes is given by $\Gamma_{vib} = 4A_u + 7B_u + 8A_g + 4B_g$. Among these modes, three correspond to acoustic vibrations ($A_u + 2B_u$), while 11 are IR-active ($4A_u + 7B_u$) and 12 are Raman-active ($8A_g + 4B_g$). The most prominent IR peaks appear at 240.90 cm^{-1} (A_u), 537.08 cm^{-1} (A_u), and 713.06 cm^{-1} (B_u). In the Raman spectrum, the most intense peaks are observed at 708.39 cm^{-1} (A_g), with additional peaks at 221.97 cm^{-1} (A_g) and 1014.01 cm^{-1} (A_g).

4. Conclusions

In this work, we conducted a thorough first-principles investigation of the molybditene monolayer, a novel two-dimensional phase of MoO_3 characterized by monoclinic symmetry (space group $P2_1/m$). Thermal stability was confirmed through ab initio molecular dynamics simulations at 300 K, which revealed no structural breakdown or phase transitions over the simulation time. Structurally, molybditene maintains its layered integrity with only minor distortions in the [MoO_6] octahedral units.

From a mechanical perspective, the elastic constants satisfy the Born–Huang criteria, and the direction-dependent analysis revealed moderate anisotropy in Young's modulus, shear modulus, and Poisson's ratio, pointing to directional mechanical response, which is advantageous for strain engineering.

The electronic band structure shows an indirect band gap with the

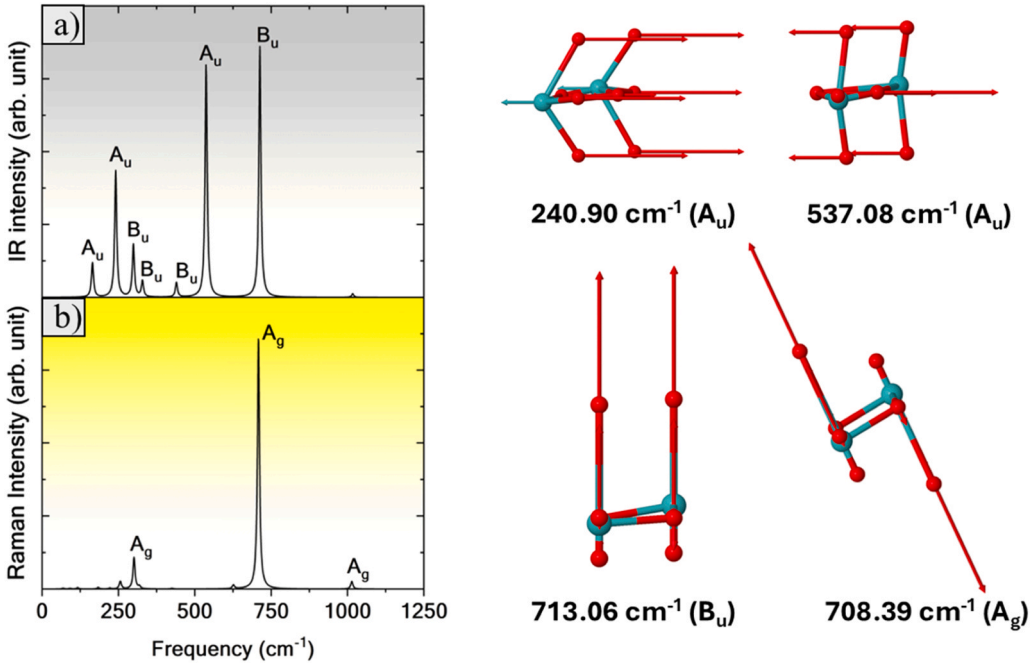

Fig. 13. Vibrational properties of molybditene. The upper panel presents the (a) infrared (IR) spectrum, while the (b) lower panel shows the corresponding Raman spectrum. The vibrations associated with the most intense peaks are showed at right.

valence band maximum located at the S point and the conduction band minimum at the Γ point. The calculated band gap varies from 1.75 eV (PBE) to 2.95 eV (HSE06), demonstrating a strong dependency on the exchange-correlation functional used.

Optical calculations reveal directionally dependent absorption and reflection spectra, with strong anisotropy between the x- and y-polarized components. The in-plane xx polarization shows strong absorption in the visible range (notably around 3.5 eV), while the yy component shows activity primarily in the ultraviolet region, reinforcing the material's potential as a polarization-sensitive optical material.

Strain engineering analyses reveal that structural and electronic properties respond distinctly to both tensile and compressive strains. While the average Mo–O bond lengths and the distortion index vary with direction and strain type, the band gap response is markedly anisotropic: moderate under ε_x, but highly tunable under ε_y, ranging from 1.10 eV to 2.30 eV. In addition, mechanical strain significantly modifies the optical properties, leading to increased anisotropy and a redshift in the absorption onset. These findings highlight the promise of molybditene for flexible electronics, strain-sensitive sensors, and polarization-selective optoelectronic applications. This tunability could be harnessed to design devices with strain-modulated optical or electronic responses, such as piezoresistive sensors or flexible photodetectors.

Funding

This work was supported by the Brazilian funding agencies Fundação de Amparo à Pesquisa do Estado de São Paulo - FAPESP (grant no. 2022/03959–6, 2020/01144–0, 24/19996–3, and 2022/16509–9), National Council for Scientific, Technological Development - CNPq (grant no. 307213/2021–8), Coordination for the Improvement of Higher Education Personnel (grant no. 88887.827928/2023–00), and Uruguay funding agencies PEDECIBA Quimica, CSIC, and ANII.

Declaration of Competing Interest

The authors declare that they have no known competing financial interests or personal relationships that could have appeared to influence the work reported in this paper.

Acknowledgments

The authors acknowledge the Molecular Simulation Laboratory and the Center for Scientific Computing (NCC/GridUNESP), both part of São Paulo State University (UNESP), Brazil, by the computational resources.

References

[1] H. Ren, S. Sun, J. Cui, X. Li, Synthesis, functional modifications, and diversified applications of molybdenum oxides micro-/nanocrystals: a review, Cryst. Growth Des. 18 (2018) 6326–6369, https://doi.org/10.1021/ACS.CGD.8B00894.

[2] A.A. Shaikh, J. Bhattacharjee, P. Datta, S. Roy, A comprehensive review of the oxidation states of molybdenum oxides and their diverse applications, Sustain. Chem. Environ. 7 (2024) 100125, https://doi.org/10.1016/J.SCENV.2024.100125.

[3] C. Cheng, A. Wang, M. Humayun, C. Wang, Recent advances of oxygen vacancies in MoO3: preparation and roles, Chem. Eng. J. 498 (2024) 155246, https://doi.org/10.1016/J.CEJ.2024.155246.

[4] S.A. Silva Lucena de Medeiros, A.L. Menezes de Oliveira, T.M. Duarte, B. J. Kennedy, A.M. Rostas, C.C. Negrila, A.C. Galca, A. da Silva Maia, J.R. Sambrano, M.C. Dantas, A.F. Felix Farias, I.M. Garcia dos Santos, α-MoO3 Micro- and nanoparticles as catalysts for biofuel production, ACS Appl. Nano Mater. 8 (2024) 4339–4353, https://doi.org/10.1021/ACSANM.4C01239.

[5] J. Wang, Y. Hu, X. Dong, Y. Wang, J. Tao, B. Yan, W. Zheng, R. Velichkova, G. Chen, Aqueous phase reforming of various compounds in biomass derived products over Ni/α-MoO3 catalysts: effect of alkali and alkaline earth metals, Fuel 359 (2024) 130388, https://doi.org/10.1016/J.FUEL.2023.130388.

[6] Y.T. Huang, L.Y. Fan, Y.F. Liu, X.H. Zheng, High-performance MoO3 nanosheets gas sensors for triethylamine detection: a rapid approach for assessing fish freshness, Ceram. Int 51 (2025) 9912–9922, https://doi.org/10.1016/J.CERAMINT.2024.12.423.

[7] H. Bai, C. Feng, Y. Chen, Y. Yan, Y. Feng, K. Liu, B. Zhang, J. Wang, D. Chen, Y. Zheng, F. Guo, Chemiresistive room temperature H2S gas sensor based on MoO3 nanobelts decorated with MnO2 nanoparticles, Sens Actuators B Chem. 420 (2024) 136468, https://doi.org/10.1016/J.SNB.2024.136468.

[8] P. Pradeep Kumar, V. Singh, Enhanced dual gas sensing performance of MoS2/MoO3 nanostructures for NH3 and NO2 detection, Ceram. Int 50 (2024) 21978–21988, https://doi.org/10.1016/J.CERAMINT.2024.03.312.

[9] Z. Lábadi, D. Takács, Z. Zolnai, P. Petrik, M. Fried, Compositional optimization of sputtered WO3/MoO3 films for high coloration efficiency, Page 1000 17, Materials 2024 17 (2024) 1000, https://doi.org/10.3390/MA17051000.

[10] H. Yu, H. Fang, K. Jing, H. Ma, L. Wu, Y. Chai, Electrochromic devices based on 2D MoO3-x/PEDOT:PSS composite film with boosted ion transport, ACS Appl. Mater. Interfaces 16 (2024) 18052–18062, https://doi.org/10.1021/ACSAMI.4C01108.

[11] R. Li, P. Song, Z. Ji, H. Zhou, X. Shen, L. Kong, A. Yuan, Flexible Ti3C2Tx MXene film coupled with Defect-Rich MoO3 Spacer-Contributor toward High-Performance wearable energy storage, Small 21 (2025) 2412250, https://doi.org/10.1002/SMLL.202412250.

[12] A.R. Patil, R.S. Desai, G.U. Kamble, A.K. Tawade, K.K.K. Sharma, J.H. Kim, D. S. Dalavi, Synthesis, analysis, and characterizations of microspherical MoO3 thin films for energy storage, Journal Materials Science Materials Electronics 35 (2024) 1–13, https://doi.org/10.1007/S10854-024-12361-6.

[13] G.S. Medeiros Leão, M.D. Silva Ribeiro, R.L. de, F. Filho, L.B. Saraiva, R.R. Peña-Garcia, A.P. de, C. Teixeira, R.M. Lago, F.A. Freitas, S. de Sá Barros, S.D. Junior, Y. L. Ruiz, F.X. Nobre, The synergic effect of h-MoO3, α-MoO3, and β-MoO3 phase mixture as a solid catalyst to obtain methyl oleate, ACS Appl. Mater. Interfaces 16 (2024) 21, https://doi.org/10.1021/ACSAMI.4C08804.

[14] Q. Qu, W.B. Zhang, K. Huang, H.M. Chen, Electronic structure, optical properties and band edges of layered MoO3: a first-principles investigation, Comput. Mater. Sci. 130 (2017) 242–248, https://doi.org/10.1016/J.COMMATSCI.2017.01.014.

[15] K.N. Amba Sankar, L. Kesavan, B. Saha, M.K. Jyolsnaraj, S. Mohan, P. Nandakumar, K. Mohanta, C. Kvarnström, Renewable synthesis of MoO3 nanosheets via low temperature phase transition for supercapacitor application, Sci. Rep. 14 (2024) 1–20, https://doi.org/10.1038/S41598-024-69765-X.

[16] P.H. Silva, D.T. Cestarolli, E.M. Guerra, Band gap values and structural changes on MoO3 obtained by ion-exchange method, Opt. Mater. (Amst.) 164 (2025) 117063, https://doi.org/10.1016/J.OPTMAT.2025.117063.

[17] A. Nagare, A. Dhadage, M. Baithy, P.M. Bhuyan, P. Gogoi, A. Athare, M. Navgire, Sol-gel assisted β-cyclodextrin coated MoO3-Fe2O3 nanocomposite for photodegradation of methylene blue dye, 2024 110:2, J. Sol. Gel Sci. Technol. 110 (2024) 304–318, https://doi.org/10.1007/S10971-024-06357-1.

[18] A. Mutlu, C. Tozlu, Electrical characterization of Ag/MoO3−x/p-Si schottky diodes based on MoO3−x synthesized via sol–gel method: an investigation on frequency and voltage dependence, Journal Materials Science Materials Electronics 35 (2024) 1–14, https://doi.org/10.1007/S10854-024-12559-8.

[19] I. Alfa, H.Y. Hafeez, J. Mohammed, A.B. Suleiman, C.E. Ndikilar, F.K. Alharbi, S. Abdu, Recent advances in enhancing MoO3-based photocatalysts for hydrogen production via water splitting, Materials 7 (2025) 100629, https://doi.org/10.1016/J.NXMATE.2025.100629.

[20] W. Guo, K. Chen, J. Wang, Hydrothermal synthesis of Zn-doped MoO3 nanoribbons with excellent triethylamine sensing performance, Journal Materials Science Materials Electronics 35 (2024) 1–13, https://doi.org/10.1007/S10854-024-12624-2.

[21] M. Khan, M. Salman, A. Ullah, N. Ullah, A. Syed, A.H. Bahkali, A. Shah, R. Ali, Y. Ling, M. Khan, Effect of hydrothermal reaction temperature on MoO3 nanostructure properties for enhanced electrochemical performance as an electrode material in supercapacitors, Ceram. Int 50 (2024) 34943–34955, https://doi.org/10.1016/J.CERAMINT.2024.06.303.

[22] T. Zima, N. Uvarov, Orthorhombic α-MoO3 nanobelts: hydrothermal synthesis and effect of treatment with an aqueous sucrose solution, NanoStruct. NanoObjects 38 (2024) 101201, https://doi.org/10.1016/J.NANOSO.2024.101201.

[23] H.T. Hsu, S.Y. Lin, Y.T. Lu, Y.Y. Chuang, S.H. Chuang, Enhanced Fenton-like process over Z-scheme MoO3 surface decorated with Fe2O3 under visible light, Sci. Rep. 14 (2024) 1–13, https://doi.org/10.1038/S41598-024-58634-2.

[24] S.M. Mir, K.R. Shaikh, A.R. Pawar, P.B. Undre, Microwave-assisted synthesis and functionalization of nanocrystalline molybdenum trioxide for enhanced antimicrobial and photocatalytic activity, J. Indian Chem. Soc. 101 (2024) 101288, https://doi.org/10.1016/J.JICS.2024.101288.

[25] Y.C. Lin, A. Kurniawan, J.A.A. Valinton, C.H. Chen, S.H. Chuang, Reduced graphene oxide-MoO3 composites via microwave-assisted synthesis for dual-functional photocatalysis of organic dyes and heavy metal cation under simulated sunlight irradiation, J. Taiwan Inst. Chem. Eng. 154 (2024) 105013, https://doi.org/10.1016/J.JTICE.2023.105013.

[26] W. Li, H. Xu, A. Wang, X. Cheng, J. Shi, A. Zhong, Y. Ma, L. Zhang, Z. Fan, F. Xu, Insitu controllable synthesis of MoO3 nanoflakes and its temperature-dependent dual selectivity for detection of ethanol and isopropanol, Sens Actuators B Chem. 408 (2024) 135548, https://doi.org/10.1016/J.SNB.2024.135548.

[27] N. Gautam, K.B. Singh, Snigdha, D.D. Upadhyay, G. Pandey, Sonochemically assisted fabrication of highly photoactive novel ZnO/MoO3 binary nanotubes anchored with Bi2O3 nanosheet for solar light-driven photocatalytic activity, J. Mol. Struct. 1306 (2024) 137812, https://doi.org/10.1016/J.MOLSTRUC.2024.137812.

[28] M. Aliannezhadi, S.Z. Mirsanai, M. Jamali, F. Shariatmadar Tehrani, Optical and structural properties of bare MoO3 nanobelt, ZnO nanoflakes, and MoO3/ ZnO nanocomposites: the effect of hydrothermal reaction times and molar ratios, Opt. Mater. (Amst.) 147 (2024) 114619, https://doi.org/10.1016/J.OPTMAT.2023.114619.

[29] Y. Hong, S. Lan, B. Pan, Z. Zhang, B. Chen, L. Zhang, P. Wang, Thinner 2D α-MoO3 makes setting up memristors easier, J. Mater. 10 (2024) 1279–1289, https://doi.org/10.1016/J.JMAT.2024.01.012.
[30] S.S. Sunu, E. Prabhu, V. Jayaraman, K.I. Gnanasekar, T. Gnanasekaran, Gas sensing properties of PLD made MoO3 films, Sens Actuators B Chem. 94 (2003) 189–196, https://doi.org/10.1016/S0925-4005(03)00342-3.
[31] Y. Wang, X. Du, J. Wang, M. Su, X. Wan, H. Meng, W. Xie, J. Xu, P. Liu, Growth of Large-Scale, Large-Size, Few-Layered α-MoO3 on SiO2 and its photoresponse mechanism, ACS Appl. Mater. Interfaces 9 (2017) 5543–5549, https://doi.org/10.1021/ACSAMI.6B13743.
[32] R. Hammad, S. Pradhan, A. Kumar, T.N. Narayanan, S. Ghosh, Heterojunction impedes ion induced metallization in 2D transition metal dichalcogenides, NPJ 2D Mater. Appl. 9 (2025) 1–7, https://doi.org/10.1038/S41699-025-00550-8.
[33] L. Boudaoud, N. Benramdane, R. Desfeux, B. Khelifa, C. Mathieu, Structural and optical properties of MoO3 and V2O5 thin films prepared by spray pyrolysis, Catal. Today 113 (2006) 230–234, https://doi.org/10.1016/J.CATTOD.2005.11.072.
[34] E.D. Hanson, L. Lajaunie, S. Hao, B.D. Myers, F. Shi, A.A. Murthy, C. Wolverton, R. Arenal, V.P. Dravid, Systematic study of oxygen vacancy tunable transport properties of Few-Layer MoO3−x enabled by Vapor-Based synthesis, Adv. Funct. Mater. 27 (2017) 1605380, https://doi.org/10.1002/ADFM.201605380.
[35] T. Nagyné-Kovács, L. Studnicka, I.E. Lukács, K. László, P. Pasierb, I.M. Szilágyi, G. Pokol, Hydrothermal synthesis and gas sensing of monoclinic MoO3 nanosheets, Page 891 10, Nanomaterials 2020 10 (2020) 891, https://doi.org/10.3390/NANO10050891.
[36] M.B. Sreedhara, H.S.S.R. Matte, A. Govindaraj, C.N.R. Rao, Synthesis, characterization, and properties of Few-Layer MoO3, Chem. Asian J. 8 (2013) 2430–2435, https://doi.org/10.1002/ASIA.201300470.
[37] C.P. Bhat, D. Bandyopadhyay, Insights into the reversible hydrogen storage mechanism of transition metal-decorated Irida-graphene: a DFT study, Int J. Hydrog. Energy 137 (2025) 750–761, https://doi.org/10.1016/J.IJHYDENE.2025.05.072.
[38] M. Crisci, P. Dolcet, J. Yang, M. Salerno, P. Bélteky, Á. Kukovecz, F. Lamberti, S. Agnoli, S. Osella, S. Gross, T. Gatti, Design principles and insights into the Liquid-Phase exfoliation of Alpha-MoO3 for the production of colloidal 2D Nano-inks in Green solvents, J. Phys. Chem. C. 126 (2022) 404–415, https://doi.org/10.1021/ACS.JPCC.1C09221.
[39] M. Sricharan, B. Gupta, S. Moolayadukkam, H.S.S.R. Matte, Exfoliation in a low boiling point solvent and electrochemical applications of MoO3, 11:52, Beilstein J. Nanotechnol. 11 (2020) 662–670, https://doi.org/10.3762/BJNANO.11.52.
[40] S. Dutta, J. Akther, S. De, Few layered MoO3 nano sheets-SWCNT composite thin film as supercapacitor electrode, AIP Conf. Proc. 1832 (2017), https://doi.org/10.1063/1.4980346/790703.
[41] F. Ji, X. Ren, X. Zheng, Y. Liu, L. Pang, J. Jiang, S. Liu, 2D-MoO 3 nanosheets for superior gas sensors, Nanoscale 8 (2016) 8696–8703, https://doi.org/10.1039/C6NR00880A.
[42] D. Hanlon, C. Backes, T.M. Higgins, M. Hughes, A. O'Neill, P. King, N. McEvoy, G. S. Duesberg, B.Mendoza Sanchez, H. Pettersson, V. Nicolosi, J.N. Coleman, Production of molybdenum trioxide nanosheets by liquid exfoliation and their application in high-performance supercapacitors, Chem. Mater. 26 (2014) 1751–1763, https://doi.org/10.1021/CM500271U.
[43] F. Ji, X. Ren, X. Zheng, Y. Liu, L. Pang, J. Jiang, S. Liu, 2D-MoO3 nanosheets for superior gas sensors, Nanoscale 8 (2016) 8696–8703, https://doi.org/10.1039/C6NR00880A.
[44] T.G. Novak, J. Kim, A.P. Tiwari, J. Kim, S. Lee, J. Lee, S. Jeon, 2D MoO3Nanosheets synthesized by exfoliation and oxidation of MoS2for high contrast and fast response time electrochromic devices, ACS sustain, Chem. Eng. 8 (2020) 11276–11282, https://doi.org/10.1021/ACSSUSCHEMENG.0C03191.
[45] H. Dou, X. You, P. Yin, X. Zhao, X. Liu, S. Liu, Y. Yang, X. Du, C. Yang, Y. Yang, Z. Niu, Y. Sun, S. Wei, P. Li, X. Zhang, Q. Jing, B. Liu, Potential high-performance H2 gas sensors based on monolayer 2D metal oxide α-MoO3 doped with Pt/Rh−predicted by DFT calculations, Int J. Hydrog. Energy 63 (2024) 10–18, https://doi.org/10.1016/J.IJHYDENE.2024.03.147.
[46] W.B. Zhang, Q. Qu, K. Lai, High-mobility transport anisotropy in few-layer MoO3 and its origin, ACS Appl. Mater. Interfaces 9 (2017) 1702–1709, https://doi.org/10.1021/ACSAMI.6B14255.
[47] Z. Tong, T. Dumitrică, T. Frauenheim, Ultralow thermal conductivity in Two-Dimensional MoO3, Nano Lett. 21 (2021) 4351–4356, https://doi.org/10.1021/ACS.NANOLETT.1C00935.
[48] G. Kresse, J. Furthmüller, Efficient iterative schemes for *ab initio* total-energy calculations using a plane-wave basis set, Phys. Rev. B 54 (1996) 11169, https://doi.org/10.1103/PhysRevB.54.11169.
[49] J.P. Perdew, Y. Wang, Pair-distribution function and its coupling-constant average for the spin-polarized electron gas, Phys. Rev. B 46 (1992) 12947, https://doi.org/10.1103/PhysRevB.46.12947.
[50] J.P. Perdew, K. Burke, M. Ernzerhof, Generalized gradient approximation made simple, Phys. Rev. Lett. 77 (1996) 3865, https://doi.org/10.1103/PhysRevLett.77.3865.
[51] G.J. Martyna, M.L. Klein, M. Tuckerman, Nosé–Hoover chains: the canonical ensemble via continuous dynamics, J. Chem. Phys. 97 (1992) 2635–2643, https://doi.org/10.1063/1.463940.
[52] Y. Zhou, W. Chu, F. Jing, J. Zheng, W. Sun, Y. Xue, Enhanced hydrogen storage on Li-doped defective graphene with b substitution: a DFT study, Appl. Surf. Sci. 410 (2017) 166–176, https://doi.org/10.1016/J.APSUSC.2017.03.057.
[53] J. Heyd, G.E. Scuseria, M. Ernzerhof, Hybrid functionals based on a screened Coulomb potential, J. Chem. Phys. 118 (2003) 8207, https://doi.org/10.1063/1.1564060.
[54] M. Ferrero, M. Ŕrat, B. Kirtman, R. Dovesi, Calculation of first and second static hyperpolarizabilities of one- to three-dimensional periodic compounds. Implementation in the CRYSTAL code, J. Chem. Phys. 129 (2008) 244110, https://doi.org/10.1063/1.3043366.
[55] A. Erba, J.K. Desmarais, S. Casassa, B. Civalleri, L. Donà, I.J. Bush, B. Searle, L. Maschio, L. Edith-Daga, A. Cossard, C. Ribaldone, E. Ascrizzi, N.L. Marana, J. P. Flament, B. Kirtman, CRYSTAL23: a program for computational solid state physics and chemistry, J. Chem. Theory Comput. (2022), https://doi.org/10.1021/ACS.JCTC.2C00958.
[56] K. Momma, F. Izumi, VESTA: a three-dimensional visualization system for electronic and structural analysis, Urn:Issn:0021-8898 41 (2008) 653–658. https://doi.org/10.1107/S0021889808012016.
[57] V. Wang, G. Tang, Y.-C. Liu, R.-T. Wang, H. Mizuseki, Y. Kawazoe, J. Nara, W. T. Geng, High-Throughput computational screening of Two-Dimensional semiconductors, J. Phys. Chem. Lett. 13 (2022) 11581–11594, https://doi.org/10.1021/acs.jpclett.2c02972.
[58] M. Gajdoš, K. Hummer, G. Kresse, J. Furthmüller, F. Bechstedt, Linear optical properties in the projector-augmented wave methodology, Phys. Rev. B Condens Matter Mater. Phys. 73 (2006), https://doi.org/10.1103/PHYSREVB.73.045112.
[59] V. Wang, G. Tang, Y.C. Liu, R.T. Wang, H. Mizuseki, Y. Kawazoe, J. Nara, W. T. Geng, High-Throughput computational screening of Two-Dimensional semiconductors, J. Phys. Chem. Lett. 13 (2022) 11581–11594, https://doi.org/10.1021/ACS.JPCLETT.2C02972.
[60] S. Imani Yengejeh, W. Wen, Y. Wang, Mechanical properties of lateral transition metal dichalcogenide heterostructures, Front Phys. (Beijing) 16 (2021) 1–7, https://doi.org/10.1007/S11467-020-1001-5/METRICS.
[61] X. Wei, B. Fragneaud, C.A. Marianetti, J.W. Kysar, Nonlinear elastic behavior of graphene: ab initio calculations to continuum description, Phys. Rev. B Condens Matter Mater. Phys. 80 (2009), https://doi.org/10.1103/PHYSREVB.80.205407.
[62] S.A. Kazemi, Y. Wang, Super strong 2D titanium carbide MXene-based materials: a theoretical prediction, J. Phys. Condens. Matter 32 (2019) 11LT01, https://doi.org/10.1088/1361-648X/AB5BD8.
[63] R. Chegel, Anisotropy in absorption and quadratic electro-optic response of monolayer boron arsenide under strain, Mater. Sci. Semicond. Process 196 (2025) 109671, https://doi.org/10.1016/J.MSSP.2025.109671.
[64] R. Chegel, Strain tuning of optical and thermoelectric properties of monolayer BAs, 2025 15:1, Sci. Rep. 15 (2025) 1–13, https://doi.org/10.1038/s41598-025-99320-1.
[65] S. Behzad, R. Chegel, Investigation of electronic properties and dielectric response of Two-Dimensional germanium selenide with puckered and buckled structures, J. Electron Mater. 51 (2022) 6275–6285, https://doi.org/10.1007/S11664-022-09817-Y.
[66] X. Bai, W. Gao, Y. Cai, Z. Bai, Y. Qi, B. Yan, Y. Wang, Z. Lu, J. Ding, Advanced stretchable photodetectors: strategies, materials and devices, Chem. A Eur. J. 29 (2023) e202203022. https://doi.org/10.1002/CHEM.202203022;CTYPE:STRING:JOURNAL.
[67] J. Du, H. Yu, B. Liu, M. Hong, Q. Liao, Z. Zhang, Y. Zhang, Strain engineering in 2D Material-Based flexible optoelectronics, Small Methods 5 (2021) 2000919, https://doi.org/10.1002/SMTD.202000919;WGROUP:STRING:PUBLICATION.
[68] X. Li, P. Li, Z. Wu, D. Luo, H.Y. Yu, Z.H. Lu, Review and perspective of materials for flexible solar cells, Mater. Rep. Energy 1 (2021) 100001, https://doi.org/10.1016/J.MATRE.2020.09.001.
[69] X. Fu, L. Xu, J. Li, X. Sun, H. Peng, Flexible solar cells based on carbon nanomaterials, Carbon N. Y 139 (2018) 1063–1073, https://doi.org/10.1016/J.CARBON.2018.08.017.